Available online at www.sciencedirect.com

SciVerse ScienceDirect

Proceedings of the Combustion Institute 34 (2013) 1609–1616

Proceedings of the Combustion Institute

www.elsevier.com/locate/proci

Sub-millimeter sized methyl butanoate droplet combustion: Microgravity experiments and detailed numerical modeling

T.I. Farouk [a,*], Y.C. Liu [b], A.J. Savas [b], C.T. Avedisian [b], F.L. Dryer [a]

[a] Department of Mechanical and Aerospace Engineering, Princeton University, Princeton, NJ 08544, USA
[b] Sibley School of Mechanical and Aerospace Engineering, Cornell University, Ithaca, NY 14853, USA

Available online 5 September 2012

Abstract

Combustion characteristics of isolated sub-millimeter sized methyl butanoate (MB) droplets are studied at low gravity (10^{-4} m/s^2) in a 1.2 s drop tower. In the experiments, droplets were grown and deployed onto the intersection of two 14 μm silicon carbide fibers in a cross-string arrangement and exposed to symmetrically placed spark ignition sources. The initial droplet diameter was fixed at 0.54 ± 0.01 mm, and experiments were carried out in room temperature air at atmospheric pressure. Detailed measurements of the evolution of droplet diameter, flame standoff ratio and burning rate are reported. The experimental results are compared against predictions from a comprehensive time-dependent, sphero-symmetric droplet combustion simulation that includes detailed gas phase chemical kinetics, spectrally resolved radiative heat transfer, multi-component diffusive transport, full thermal property variations and tether fiber perturbation effects. The predicted combustion characteristics of MB are also compared with *n*-heptane droplets of nearly identical sizes over a range of oxygen concentrations.

The results show that predicted burning histories, burning rates and flame standoff ratios are in excellent agreement with the measurements. The average burning rates and flame temperatures for both fuels were found to be similar even though the heat of combustion of *n*-heptane is higher by a factor of ~1.6. However, the average flame standoff ratio for MB was found to be significantly smaller than for *n*-heptane, due to the presence of additional oxygen atoms in the parent fuel. Important differences in the diffusion flame chemistries of the two fuels are also discussed.

Keywords: Methyl butanoate; Biodiesel; Droplet combustion; Microgravity; Modeling

1. Introduction

Biodiesel is a renewable fuel source suitable for use within the current transport sector infrastructure, as it shares similar physical properties with conventional petroleum-derived diesel fuel. Biodiesel is a mixture of saturated and unsaturated alkyl esters containing carbon chains of 12–24 atoms in length produced by transesterification of various plant oils. As a result of the high boiling point, fundamental research on this nearly "carbon neutral" [1] fuel is difficult. Fuel vaporization can be accompanied by decomposition reactions, and the detailed kinetics present

* Corresponding author. Current address: Department of Mechanical Engineering, University of South Carolina, Columbia, SC 29208, USA. Fax: +1 609 258 5206.
E-mail addresses: tfarouk@princeton.edu (T.I. Farouk), tanvir.farouk@gmail.com (T.I. Farouk).

1540-7489/$ - see front matter © 2012 The Combustion Institute. Published by Elsevier Inc. All rights reserved.
http://dx.doi.org/10.1016/j.proci.2012.07.074

difficulties in development and validation as a result of the large numbers of species and reactions [2]. Previous work [3] utilized detailed chemical kinetic studies of methyl butanoate (MB) and methyl formate (MF) as simpler species for study of the ester group affects on combustion chemistry. Though the carbon chain of MB is insufficient for producing the two stage kinetics typically observed with larger carbon number esters [4], the high temperature kinetics of the ester group can be reasonably investigated by studying MB.

Substantial fundamental research on pre-vaporized combustion of MB has appeared, including its auto ignition behavior in reflected shock and rapid compression machine configurations [5], oxidative species evolutions in a jet stirred reactor (JSR) [6], a variable pressure flow reactor (VPFR) [6] and opposed flow diffusion flame [6,7] experiments, and extinction strain rate measurements in counter flow diffusion flames [8]. Here, we report on the multi-phase combustion characteristics of isolated liquid MB droplets in quiescent, oxidizing environments to generate insights into the transient physico-chemical processes that are involved in liquid and gas phase coupled combustion. Low gravity, isolated droplet burning experiments are utilized to achieve nearly spherically symmetric burning behavior. This experimental configuration is conducive to quantitative temporal and spatial measurements of various combustion targets (e.g. burning rate (K), flame standoff ratio (FSR)) as well as gas phase species (e.g. OH, soot) by use of optical diagnostics. Moreover, this simple two-phase, time dependent combustion configuration permits numerical modeling with detailed chemical kinetics, multi-component diffusive transport, and spectral radiative sub-models.

This paper presents the results of microgravity MB droplet experiments conducted in a 1.2 s drop tower, and compares observations against detailed numerical predictions. The combustion characteristics of MB droplets are also compared with previously published *n*-heptane (nH) droplet combustion results [9] for which the experimental conditions were almost identical to those of the present experiments. Simulation results of burning MB and nH droplets are compared over a range of oxygen concentrations to elucidate the variation in the average burning rate (K_{avg}), average flame standoff ratio (FSR_{avg}), average flame temperature (T_{avg}), and extinction diameter (D_e) with fuel type. Insights as to differences in kinetic aspects of the two fuels are also presented.

2. Experimental setup and procedure

Individual MB droplets are formed, deployed, and ignited under conditions that achieve nearly sphero-symmetric, concentric burning conditions. The MB used in the experiments was 99% pure, supplied by Aldrich. A piezoelectric generator [10] is used to direct fuel droplets onto two 14 μm SiC fibers, crossed at approximately 60° (see Fig. 1a, a planar view), until the droplet reaches the desired size ($D_o \sim 0.54$ mm). The droplet generator, electrodes and support fibers are mounted in a sealed chamber containing room temperature air at atmospheric pressure. Once the desired droplet size is produced, the package is released into free-fall. Gravity levels on the order of 10^{-4} of Earth's normal gravity are achieved during the fall with the aid of a drag shield [11]. Approximately 320 ms into the fall, the droplet is ignited by two spark ignition sources (of 800 μs duration) symmetrically placed about the droplet [12] that are then retracted to the far field.

Two orthogonal views of the droplet burning process are recorded. A color video camera (Hitachi HV-C20 operated at 30 frames per second with a Nikkor 135 mm f/2.0 lens and two Kenko 36 mm extension tubes) recorded self-illuminated flame images. A black and white (BW) digital camera (3.9 MP per frame Canadian Photonics Labs, Inc. MS-80K digital high speed camera operated at 200 fps, and fitted with an Olympus Zuiko 90 mm f/2.0 lens, an Olympus OM Telescopic Extension Tube 65–116 mm (fixed at 100 mm), and a Vivitar MC 2X teleconverter) recorded the (backlighted) evolution of droplet diameter. Backlighting was provided by a 1-Watt LED lamp (Black Diamond Equip, LTD). Four separate repetitions having identical initial conditions were performed to examine experimental repeatability.

Droplet diameters (D) are obtained using a frame-by-frame analysis of individual digital images using a MATLAB-based algorithm [13]. Flame diameters are determined from the color images using CorelDraw 9, in which a digital ellipse is visually positioned around the outer luminous zone of the flame to yield an equivalent flame diameter. The uncertainty in the droplet and flame diameter measurements was dictated by the number of pixels the image encompassed. Therefore higher uncertainty exists for smaller droplet and flame sizes. Further details on the experimental methods, image processing and discussion of the experimental uncertainty appear elsewhere [9].

3. Numerical modeling

The experimental results are compared against predictions from an independently developed comprehensive numerical model that has been described in detail elsewhere [14,15]. The transient, spherically symmetric droplet combustion model features detailed gas phase kinetics, spectrally resolved radiative heat transfer, multi-component gas transport and heat transfer

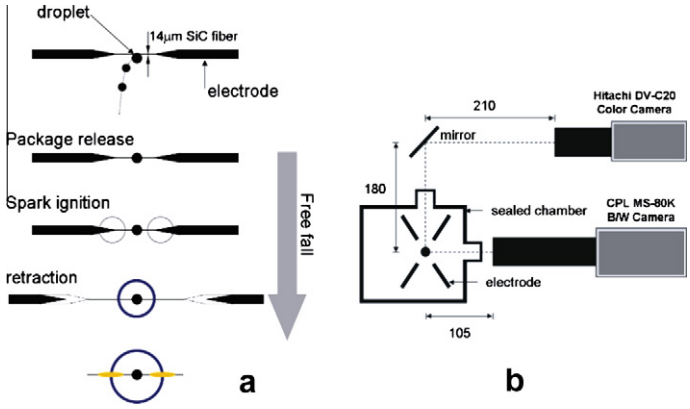

Fig. 1. (a) Schematic of experimental procedure to deploy droplets onto a 14 μm SiC fiber in a cross string arrangement, involved in a droplet combustion experiment with reduced convection. (b) Experimental setup (numbers in millimeters) not to scale.

perturbations due to the presence of the tether fibers. It is expected (and therefore assumed) that no dissolution of gas phase species occurs at the gas liquid interface for these fuels studied. Mass and energy conservation is solved in both the gas and liquid phase. The heat transfer within the droplet is of "finite" conduction prescribed by the liquid phase thermal conductivity. The data correlations of Daubert and Danner [16] were used to calculate the liquid phase properties. The properties of the SiC tether fiber used for the simulations were $\rho_f = 2740\ \mathrm{kg/m^3}$, $c_{p,f} = 670\ \mathrm{J/kg\,K}$, $k_f = 5.2\ \mathrm{W/m\,K}$ [17] and $\varepsilon = 1.0$. The detailed kinetic models of Dievart et al. [4] for MB and Chaos et al [18] for *n*-heptane were used in the simulations without further reduction. The *n*-heptane model was modified by appending the PAH sub-mechanism of Raj et al. [19] in order to consider the potential for the formation of higher molecular weight species within the *n*-heptane diffusion flames.

In the simulations, Dirichlet conditions of fixed ambient composition (fixed O_2 and N_2 composition) and temperature (298 K) are imposed on the far-field. In prior simulations of hot wire ignition [20], a symmetric region of trapezoidal shape with a peak temperature of 2000 K located 0.5 mm away from the droplet surface was provided as the initial condition to simulate the experiments, and the ignition parameters were found to have little effect on the predictions. Spark ignition adds far less overall enthalpy to the surroundings and droplet than is characteristic of hot wire ignition observations. At much reduced ignition energy conditions, ignition simulation parameters significantly influence the predicted initial stage of droplet burning rate behavior namely; a slower transition to quasi-steady state.

Figures 2a and b compare the predicted evolution of D and K (discussed in more detail in Section 4) with the experiments for two different ignition energy configurations (see Fig. 2 inset). The ignition energy is prescribed by the energy density $(\rho c_p \Delta T)$ of the initially prescribed

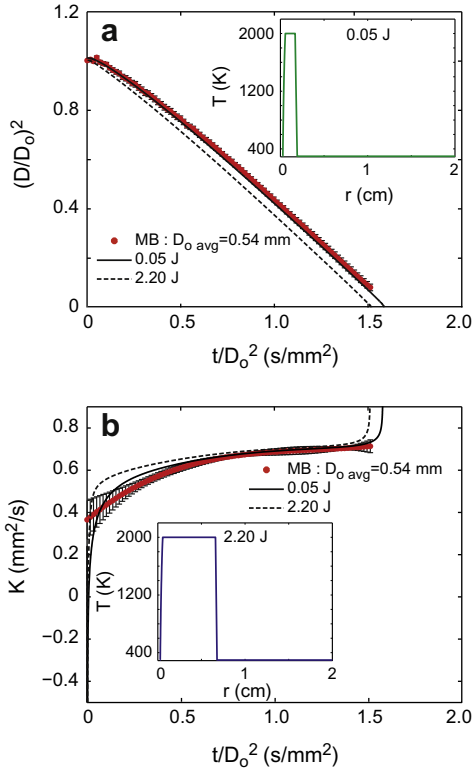

Fig. 2. Influence of initial ignition energy on evolution of (a) droplet diameter and (b) burning rate for a methyl butanoate (MB) droplet ($D_o = 0.54$ mm, atmospheric air). Predictions are compared with measurements. The MB data shown are the average of 4 individual runs and are identical to that presented in Figs. 4b and 5b.

temperature profile integrated over the trapezoidal-shaped region depicted in the figures. It is important to note that a spark is the result of an equilibrium thermal plasma discharge, where the plasma forms a uniform cylindrical columnar channel in between the electrodes and has a gas temperature of ~2000 K [21]. On this basis, a trapezoidal profile with a peak temperature of 2000 K is a reasonable gross approximation for the ignition source. The spark energy of 50 mJ and duration of ~800 microseconds was imposed in the model in order to be consistent with the spark energy of the experiment. To simulate a hot wire type igniter the ignition energy is increased substantially, retaining a similar temperature profile shape to maintain modeling concepts of the two different cases. Shaw et al. [12] showed in their work that a hot wire ignition process adds far more energy to the gas phase and the liquid droplet during the ignition process than does spark ignition; modifying the initial droplet heating transient associated with the ignition process. Both the predicted D and K are in excellent agreement with the measurements for an ignition energy of 0.05 J. For the ignition parameters prescribed earlier for hot wires (2.20 J), the dissipated energy influences a larger volume of the ambience, enhances initial droplet heating, and affects the initial burning rate behavior (Fig. 2b), showing a substantially rapid transition to quasi-steady state. D^2 regresses linearly almost from the onset of burning for the 2.20 J case, while for the 0.05 J case, the initial stage of gasification and droplet heating approach quasi-steady burning only after about 40% of the total burn time. After achieving quasi-steadiness, the D^2 regression rate is nearly independent of earlier transients.

4. Results and discussion

The evolution of the droplet burning process is shown by the exemplar set of photographs in Fig. 3 from the digital video records. Some initial asymmetry of the flame structure exists due to gas motions induced by spark ignition and electrode retractions, though the flame shapes were largely spherical throughout the burning process. As illustrated in Fig. 3a, soot formation is not observed (i.e., no soot shell). The sequence of color images (Fig. 3b) show a faint blue luminosity indicative of CH emissions which is also consistent with no soot formation.

Figure 4a shows quantitative measurements of the evolution of droplet diameter of individual experimental runs in the coordinates of the classical D^2 law. The trends show a transient burning behavior that extends up to 40% of the total burn time after which quasi-steady burning results independent of the earlier transient behavior. This is more clearly seen in Fig. 4b which shows the data of Fig. 4a averaged over the four individual runs, along with error bars on the measurements (mean and standard deviation). Also included in Fig. 4b are measurements from [9] for nH droplets for $D_o = 0.50$ mm (average experimental values). Table 1 presents the property differences between MB and nH. The differences in the thermal conductivities and heat capacities are reflected in the heating of the droplets to their saturation temperatures. Unlike alcohols, dissolution of gas phase species does not occur at the gas liquid interface for MB and nH. Therefore multi-component transport and mixing is not considered in the liquid phase. As stated earlier, soot formation is considered only for the nH cases. The comparison between the measurements and numerical simulations is excellent for both fuels. The predicted diameter evolutions show evidence of early thermal expansion of the droplets, consistent with experimental observations. Both droplets burn to completion as observed experimentally. nH appears to burn at a slightly faster rate (~6%), though nH's heat of combustion (ΔH_c) is 40% higher than that of MB (Table 1).

The peak temperature evolution is presented using a logarithmic time scale to provide insight into the temporal progression at the small time scales. The predicted maximum gas temperatures (T_{max}) in Fig. 4b show that the T_{max}s initially decrease due to the initial heating of the droplet, endothermic fuel vapor reactions and heat loss to the ambience. The decrease is greater for MB than for nH, mostly because of differences in heat capacity and latent heat of vaporization (Table 1). The decreases are followed by sharp increases, indicating ignition of the fuel-air vapor mixture surrounding the droplet. Subsequently, the temperatures decrease as the flame structure transitions to that of a quasi-steady burning condition involving sustained liquid fuel vaporization and continued loss of heat through diffusion to the ambience. With similar ignition energy inputs, MB takes longer to ignite, with a quasi-steady flame temperature of only ~40 K lower than nH despite the large difference in ΔH_c.

Figure 5a shows the evolution of the burning rate obtained by fitting the data in Fig. 4a to 4th order polynomials and taking the first derivative. Even though the K data fall along a small band during most of the initial stages of burning, large variations are observed for nearly identical D_o early in the burning history. These are likely due to stochastic variations in the paths of arcing at ignition as well as from electrode retraction disturbances of the surroundings.

Figure 5b shows the evolution of burning rate constants (obtained by fitting the average D^2 profiles shown in Fig. 4b) and predictions from the detailed numerical model that includes simulations for nH. The predicted K evolution shows a large negative value at the initial state of the burn

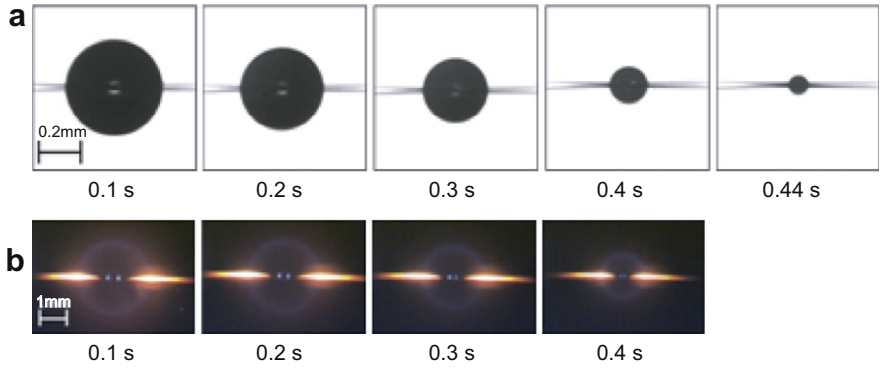

Fig. 3. (a) Selection of BW images for a burning methyl butanoate (MB) droplet in atmospheric air. (b) Color images of droplet in "a" showing the flame structure (glow is due to flame/fiber interaction). Representative length scales for the droplet and flame images are also provide. Note the differences in scale between "a" and "b" (0.2 mm for droplet and 1.0 mm for flame images).

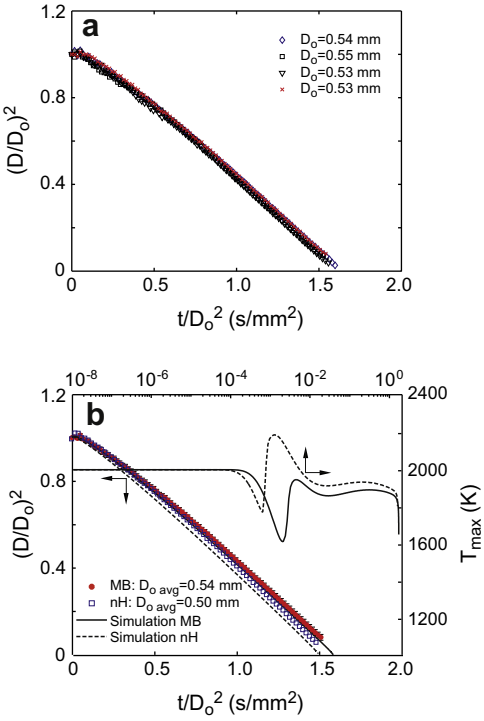

Fig. 4. (a) Evolution of methyl butanoate (MB) droplet diameter showing trends for four individual runs (atmospheric air), (b) comparison of measured and predicted droplet diameters and predicted peak temperature for MB and *n*-heptane (nH) [9]. The secondary axes (upper logarithmic and right hand) represent the temperature evolution. The logarithmic scale provides insight into the temperature evolution at the small time scales. The MB data in "b" are averaged from the 4 runs in "a".

occurring as the droplet diameter increases due to thermal expansion. A sharp rise in K occurs towards the end of the burn as the droplet diameter becomes comparable to the fiber diameter with additional heat flux from the fibers becoming significant. The time-averaged experimental and predicted Ks for MB and nH differ by less than 3% (averaging was performed for values in between $0.10 \leq t_b \leq 0.90$, where t_b is the total burn time).

Figure 6a shows the evolution of the *FSR* for the individual sub-millimeter sized droplets studied here. Figure 6b depicts the *FSR* data of Fig. 6a averaged over the four individual runs, along with error bars on the measurements (mean and standard deviation) together with measurements for nH [9]. Error bars are shown to illustrate the uncertainty. The trends show a continually increasing *FSR* due to thermal buffering of the far field that leads to decreased loss of heat from the flame structure and an ever increasing *FSR* as burning progresses. Figure 6b also shows the predicted *FSR* evolution; predictions of the flame position marked by the location of T_{max} [14]. The model predictions agree well with experimental observations and are within the uncertainty limits of the measurements. The flame resides where the fuel and oxidizer are at the stoichiometric condition. The reduced oxygen coefficient for stoichiometric MB combustion versus that for nH (Table 1) leads to a reduced *FSR*, compensating for the lower ΔH_c of MB and resulting in essentially identical burning rates (cf. Fig. 5) and quasi steady maximum flame temperatures.

To further elucidate the relative flame structures of MB and nH, computations were performed for a broad range of ambient oxygen concentrations ($0.09 \leq X_{O_2} \leq 0.5$). Figure 7 presents the predicted K_{avg}, T_{avg}, FSR_{avg} and the normalized extinction diameter (D_e/D_o) as a function of X_{O_2} for the combustion of identical MB and nH droplet sizes. All the predicted K_{avg}, T_{avg},

Table 1
Selected properties of methyl butanaote (MB) and *n*-heptane (nH) [23].

Property	MB $C_5H_{10}O_2$	nH C_7H_{16}
Molecular weight, M_w (g/mol)	102.1	100.2
Boiling point, T_b (K)	376	372
Density*, ρ_l (kg/m^3)	898.4	679.5
Specific heat*, $c_{p,l}$ (kJ/kg)	1.941	2.242
Thermal conductivity*, k_l (W/mK)	0.1403	0.1235
Heat of vaporization, ΔH_v @T_b (kJ/mol)	141.4	132.9
Heat of combustion, ΔH_c (kJ/mol)	2945.5	4849.2
Measured average burning rate, $K_{avg\ expt}$ (mm^2/s)	0.64	0.67
Predicted average burning rate, $K_{avg\ sim}$ (mm^2/s)	0.65	0.69
Stoichiometric coefficient	7.5	11.0

* Values of density and specific heat are @ 298 K.

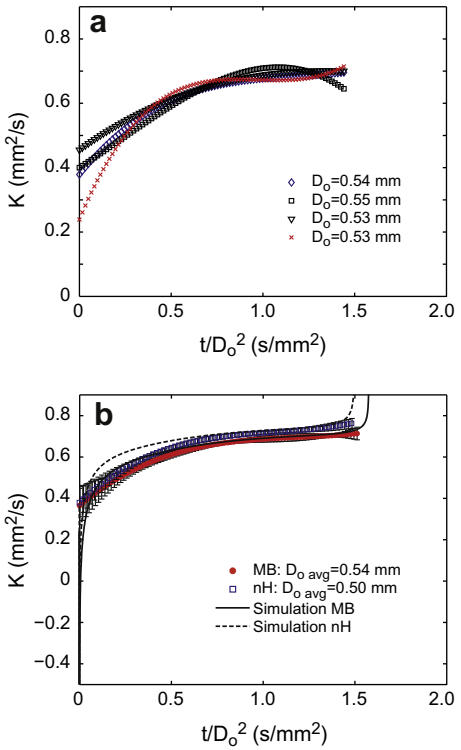

Fig. 5. (a) Evolution of burning rate of methyl butanoate (MB) droplets of the indicated initial diameters (atmospheric air), (b) comparison of measured and predicted burning rates for MB and *n*-heptane (nH) [9]. The MB data in "b" are averaged from the 4 runs in "a".

FSR_{avg} are obtained by time averaging the predicted values in between $0.10 \leq t_b \leq 0.90$. These average quantities provide insight into the quasi-steady combustion characteristics. Increasing X_{O_2} increases the burning rate by increasing the flame temperature (Fig. 7a). FSR_{avg} decreases

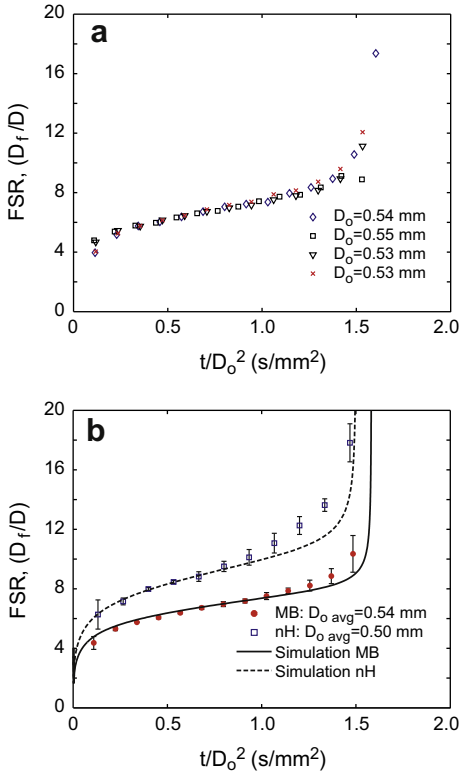

Fig. 6. (a) Evolution of *FSR* for four individual runs of methyl butanoate (MB) droplets for the indicated initial droplet diameters (atmospheric air), (b) comparison of measured and predicted *FSR* for MB and *n*-heptane (nH) [9]. The MB data in "b" are averaged from the 4 runs in "a".

with increasing X_{O_2}, as stoichiometric conditions are achieved nearer the droplet surface. As the limiting oxygen index (LOI) is approached, the FSR_{avg}s decrease due to an inability to achieve quasi-steady burning conditions. Extinction for these sub-millimeter droplets starts occurring at $X_{O_2} = 0.15$ for MB and $X_{O_2} = 0.13$ for nH, with sharp increases in extinction diameter as LOIs are approached. In comparison, the extinction diameter for MB was found to be always higher than that of nH for the same ambient oxygen concentration. MB and nH have distinctly different FSR_{avg} and extinction characteristics though their K_{avg} and T_{avg} are close.

The evolution of maximum ethylene (C_2H_4), acetylene (C_2H_2) and formaldehyde (CH_2O) mass fraction for identical MB and nH droplet burning conditions are presented in Fig. 8. Both fuels are predominantly decomposed in the droplet burning process by H abstraction/alkyl/radical beta-scission reactions. Hydrogen atom is the principle abstractor, consuming 80% and 86% of the fuel respectively in nH and MB droplet flames. Although the generic mechanism of fuel

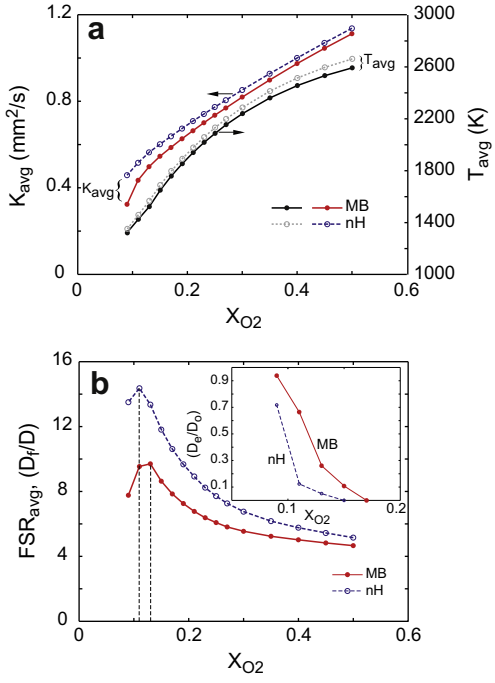

Fig. 7. Predicted average (a) burning rate, flame temperature and (b) *FSR*, normalized extinction diameter (D_e/D_o) as a function of ambient oxygen mole fraction for identical methyl butanoate (MB) and *n*-heptane (nH) droplets ($D_o = 0.55$ mm, varying O_2/balance N_2, 1 atm, free floating). The average values are obtained by time averaging the predicted values in between, $0.10 \leqslant t_b \leqslant 0.90$ where t_b is the total burn time.

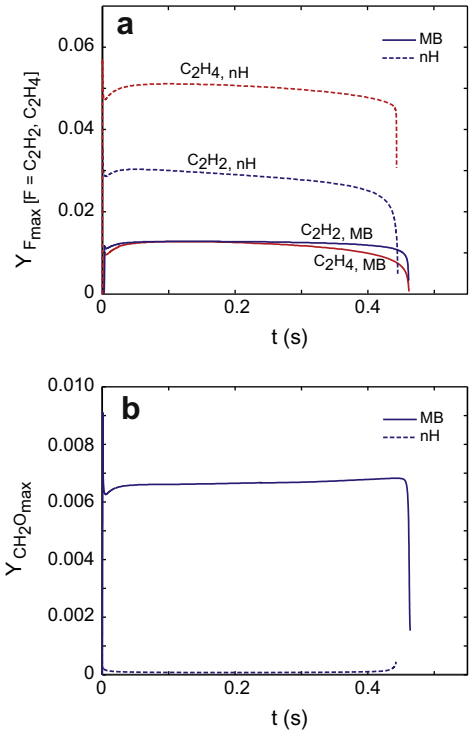

Fig. 8. Predicted evolution of peak (a) C_2H_4, C_2H_2 and (b) CH_2O mass fraction for identical methyl butanoate (MB) and *n*-heptane (nH) droplets burning in 0.21 X_{O_2} ($D_o = 0.55$ mm, varying O_2/balance N_2, 1 atm, free floating).

consumption is similar for nH and MB, it is noteworthy that the intermediate species formed differ considerably being dependent on the parent fuel chemistry. The radicals formed by abstraction produce principally C_2 species in the case of nH, while formaldehyde is the main beta scission product in the MB flame. C_2H_4 and C_2H_2 concentrations are factors of 5 and 3 lower in the MB case, while formaldehyde is a secondary product from CH_3 reactions in the nH flame.

Most of the C_2H_4 formation in nH takes place directly from the fuel through the beta scission of the alkyl radical ($nC_7H_{15} \rightarrow nC_5H_{11} + C_2H_4$). Ethylene is the most prominent intermediate in the oxidation of nH, which unlike MB forms high concentration of C_2H_4 instead of CH_2O. Large amounts of C_2H_4 also promote the formation of vinyl radicals (C_2H_3). The consumption pathways of C_2H_3 result in the formation of the other two intermediates acetylene and propylene (C_3H_6) not shown here; $C_2H_3 + H = C_2H_2 + H_2$, $C_2H_3 + CH_3 = C_3H_6$. All these intermediates are found to form in the fuel rich side of the diffusion droplet flame structure [14,22]. The relative difference in the presence of C_2 species on the fuel rich side of the MB and nH diffusion flame structures indicate that MB has a much lower propensity to soot under the same droplet burning conditions than does nH, which is confirmed by the experimental observations (cf. Fig. 3).

Figure 8b shows the temporal evolution of peak CH_2O for MB and nH. Compared to nH diffusion flames, MB diffusion flames form significantly larger amounts of CH_2O, up to a factor-of-three higher in peak values relative to nH. Formaldehyde results from H abstraction/beta scission of the MB fuel structure, where as its production in nH flames results from the small species reactions in the reaction zone (stoichiometric conditions), somewhat after the nH has been consumed. For nH, the dominant CH_2O production pathway is through the oxidation of methyl (CH_3) radical via O atom and OH radical, occurring in the reaction zone. For MB, the significant CH_2O production comes from the decomposition of MB radical fragments, which locate the peak CH_2O concentration in the fuel rich side. Consumption of CH_2O through H abstraction produces formyl (HCO) radicals. Formation of peroxy (HO_2) radicals ($HCO + O_2 = HO_2 + CO$) goes through radical chain termination reactions resulting in extinction similar to that observed in counter flow diffusion flames [8]. The difference

in formaldehyde intermediate concentration is relevant to the differences in extinction characteristics for the two fuels.

5. Summary

Sphero-symmetric, isolated MB droplet combustion was studied experimentally. The MB data were compared against predictions from a comprehensive numerical model of droplet combustion, as well as with similar sized nH droplet burning data. The experiments and model results showed very good agreement.

Measured droplet diameter regression and computed burning rates showed significant nonlinearity, in some cases extending through more than ~40% of the burn time, with an eventual establishment of quasi-steady burning behavior. For atmospheric pressure air, and the droplet size studied, burning of MB droplets occurred without soot formation and to completion. Burning characteristics of MB were compared with nH and the results were found to be very similar, with the exception of the *FSR* histories of each fuel despite the large differences in their heats of combustion.

Model predictions identified that the transient burning behavior for the MB experiments results from reduced droplet and environmental heating associated with the use of low energy spark compared to hotwire ignition. Model predictions were in very good agreement with the measured droplet diameter regression, burning rate and flame standoff ratio observations for MB and nH. The average burning rate and flame temperature for identical MB and nH droplets were found to be very similar even though the heat of combustion of nH is higher by a factor of ~1.6. However the *FSR* for a MB droplet was found to be significantly smaller due to the presence of oxygen in the fuel resulting in increased heat feedback to the droplet and reduced heat loss to the ambient.

Analysis of the kinetics within nH and MB droplet flame structures showed that MB produces significantly lower amounts of C_2 hydrocarbon intermediates and much higher amounts of formaldehyde. The reduced presence of C_2 hydrocarbon intermediates proffers reduced sooting in the case of MB diffusive combustion, while the higher concentration of formaldehyde is believed to be responsible for the observed differences in diffusive extinction between MB and nH.

Acknowledgements

This work was supported by the National Aeronautics and Space Administration through grant numbers NNX09AW 19A (for TF and FLD) and NNX08AI51G (for YCL, AJS and CTA). Special thanks go to Mr. Michael Hicks and Dr. Daniel Dietrich of NASA for their interest and assistance throughout the course of this investigation.

References

[1] G. Knothe, *Fuel Process. Technol.* 86 (2005) 1059–1070.
[2] O. Herbinet, W.J. Pitz, C.K. Westbrook, *Combust. Flame* 157 (2010) 893–908.
[3] E.M. Fisher, W.J. Pitz, H.J. Curran, C.K. Westbrook, *Proc. Combust. Inst.* 28 (2000) 1579–1586.
[4] P. Dievart, S.H. Won, S. Dooley, F.L. Dryer, Y. Ju, *Combust. Flame* 159 (5) (2012) 1793–1805.
[5] S. Dooley, H.J. Curran, J.M. Simmie, *Combust. Flame* (2008) 153 (1-2), 2-32.
[6] S. Gail, M.J. Thomson, S.M. Sarathy, et al., *Proc. Combust. Inst.* 31 (2007) 305–311.
[7] S.M. Sarathy, S. Gail, S.A. Syed, M.J. Thomson, P. Daguat, *Proc. Combust. Inst.* 31 (2007) 1015–1022.
[8] S. Dooley, M. Uddi, S.H. Won, F.L. Dryer, Y. Ju, *Combust. Flame* 159 (4) (2012) 1371–1384.
[9] Y.C. Liu, C.T. Avedisian, *Combust. Flame* 159 (2012) 770–783.
[10] C.T. Avedisian, J.C. Yang, C.H. Wang, *Proc. R. Soc. Lond. Ser. A Math. Phys. Eng. Sci.* 420 (1988) 183–200.
[11] G. Jackson, C.T. Avedisian, *Proc. R. Soc. Lond. Ser. A Math. Phys. Eng. Sci.* 446 (1994) 255–276.
[12] B.D. Shaw, F.L. Dryer, F.A. Williams, N. Gat, *Combust. Flame* 74 (1988) 233–254.
[13] C. Dembia, Y. C. Liu, C.T. Avedisian, *Image Analysis and Stereology*, in press.
[14] T. Farouk, F.L. Dryer, *Combust. Theor. Model.* 15 (4) (2011) 487–515.
[15] T. Farouk, F.L. Dryer, *Combust. Flame* 159 (2012) 200–209.
[16] T.E. Daubert, R.P. Danner, *Physical and Thermodynamic Properties of Pure Chemicals: Data Compilation*, Hemisphere Publishing, New York, 1989.
[17] M. Mikami, H. Oyagi, N. Kojima, M. Kikuchi, Y. Wakashima, S. Yoda, *Combust. Flame* 141 (2005) 241–252.
[18] M. Chaos, A. Kazakhov, Z. Zhao, F.L. Dryer, *Int. J. Chem. Kinet.* 39 (2007) 399–414.
[19] A. Raj, I.D.C. Prada, A.A. Amer, S.H. Chung, *Combust. Flame* 159 (2012) 500–515.
[20] D. Dietrich, Technical Publication NASA/TP-2011-xxxx (2011) NASA, Glenn Research Center, Cleveland OH 44135, USA, December 2011.
[21] R. Ono, M. Nifuku, S. Fujiwara, S. Horiguchi, T. Oda, *J. Appl. Phys.* 97 (2005), 123307-7.
[22] A.J. Marchese, F.L. Dryer, V. Nayagam, *Combust. Flame* 116 (1999) 432–459.
[23] D.R. Lide, W.M. Haynes, *CRC Handbook of Chemistry and Physics*, 90th ed., FL, Boca Raton, 2010.